Finite/Discrete Element Method (FDEM) by Y-Geo: An overview

Murad S. Abuaisha, David Eaton, Jeffrey Priest, Ron Wong

Chapter 7

Finite/Discrete Element Method (FDEM) by Y-Geo: An overview

Murad AbuAisha[a,b]*, David W. Eaton*[a]*, Jeffrey Priest*[b] *and Ron Wong*[b]
[a] *Dept. of Geoscience, Univ. of Calgary, Calgary, AB, T2N 1N4, Canada.*
[b] *Dept. of Civil Engineering, Univ. of Calgary, Calgary, AB, T2N 1N4, Canada.*
E: murad.abuaisha@ucalgary.ca

Summary

This paper discusses the issues involved in the development of combined finite–discrete element methods (FDEM), from a fundamental theoretical point of view and some related algorithmic considerations essential for the efficient numerical solution of large scale industrial problems.

Starting from a continuum representation by finite elements of the solid region in question, progressive fracturing is allowed to take place according to some fracturing criterion, thereby forming discrete elements, which may be composed of one or more deformable finite elements. Subsequent motion of these discrete elements and further fracturing of both remaining continuum and previously created discrete elements is then modelled. This evolution process is continued until either the system comes to rest.

Y–Geo is a new numerical code for geomechanical applications based on the combined continuum/discontinuum modeling. Several algorithmic developments have been implemented in Y–Geo to specifically address a broad range of rock mechanics problems. These features include (1) a quasi–static friction law, (2) the Mohr–Coulomb failure criterion, (3) a rock joint shear strength criterion, (4) a dissipative impact model, (5) an *in situ* stress initialization routine, (6) a material mapping function (for an exact representation of heterogeneous models), and (7) a tool to incorporate material heterogeneity and transverse isotropy.

7.1 Introduction

This paper deals with hydraulic fracturing, a technique mainly used in the petroleum industry to enhance the recovery of oil and gas from underground hydrocarbon reservoirs. Other applications include (but are not limited to) underground disposal of liquid toxic waste, determination of *in situ* stresses in rock, and creation of geothermal energy reservoirs, AbuAisha (2014).

Hydraulic fracturing consists of injecting a viscous fluid into a well under high pressure to initiate and propagate a fracture. The design of a treatment relies on the ability to predict the opening and the size of the fracture as well as the pressure of the fracturing fluid, as a function of the properties of the rock and the fluid. In that respect, the availability of numerical approaches to solve hydraulic stimulation problems is especially valuable. The construction of such approaches, for the particular method of continuum/discontinuum modelling, is the topic of this paper.

Geomaterials are made of small–structural elements and fracture occurs through alteration, damage, yielding or failure of these elements. The alteration of stress and strain fields due to the presence of such small–structures must be taken into account in order to describe this complex material dependent phenomenon of fracturing. In linear elasticity this can be represented by the singularity of the stress field at the crack tip. However, the assumption of continuum media is only valid for sufficiently large volumes, i.e. on the scale much larger than the representative volume. The combination of continuum/discontinuum modelling through the Finite–Discrete Ele-

ment Method (FDEM) has proven to be a valuable tool to describe fracturing in geomaterials, Munjiza et al. (1995).

The combined finite–discrete element method involves extensive fracture and fragmentation (in applications such as rock blasting) resulting in a large number of individual solid fragments, i.e. it is characterized by systems comprising a large number of separate (distinct) deformable bodies (called discrete elements), which move in space and time interacting with each other with each individual body discretized into finite elements. In the context of the combined finite-discrete element method robustness, accuracy, simplicity and CPU requirements of the fracture algorithm implemented are therefore of major importance, Mahabadi et al. (2012).

To describe fracture evolution in FDEM, the local approaches based on a single crack model are used. The model is a relatively simple non–linear for a crack with a plastic zone at its tips (FPZ), where the zone of plastically strained material is replaced by a zone of weakened bonds between the crack walls (Fig. 1). As the crack walls separate the bond stress reaches maximum f_t. At the point when the separation reaches critical value $\delta = \delta_c$ the bonding stress drops to zero, Lu and Chow (1990).

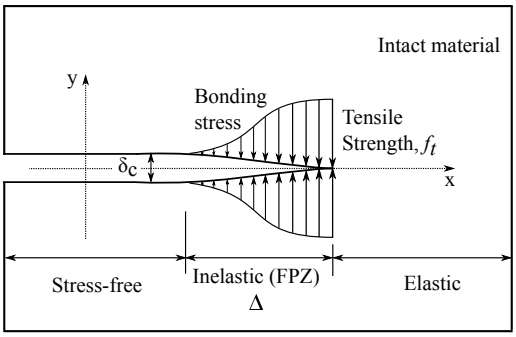

Figure 1: Conceptual model of a tensile crack in a heterogeneous rock material – Dugdale crack model, Lu and Chow (1990).

To present fracturing of brittle materials, the aforementioned model is implemented using experimental stress–strain curves for concrete in tension, Hillerborg mode – Hillerborg et al. (1976). The standard finite element formulation for the hardening part of the constitutive low is combined with the single–crack model for the softening part of the stress–strain curve. Finite elements are used to model the behavior of the material up to the ultimate tensile strength while a discrete crack model is implemented through crack opening and separation along edges of finite elements. The major advantages of the proposed model are its ability to model both crack propagation and crack initiation of multiple cracks allowing creation of large numbers of distinct interacting fragments without considerable additional CPU requirements, i.e. remeshing.

The first objective of this research is to illustrate the conception of the fracturing model to be used in the FDEM and then coded in the Y–Geo. Such illustration is to include; 1- the constitutive behavior of the model and the crack elements in a single and smeared fracturing approaches, 2- the governing equations and their matrix formulation, 3- the numerical integration scheme, 4- the spatial discretization, and finally the implementation of fluid pressure/hydraulic stimulation in the fracturing model. The second objective is to scrutinize the limitations and concerns of the FDEM approach implemented in the Y-Geo code.

7.2 Combined single and smeared fracturing

The model introduced in this work is aimed at crack initiation and crack propagation in geomaterials in the context of the combined finite–discrete element method FDEM. The model is able to track the evolution of a single–crack as well as of a group of possibly interacting cracks – smeared fracturing. The model is based on actual approximation of experimental stress–strain curves for concrete in direct tension, Evans and Marthe (1968). The area under the stress–strain curve, (Fig. 2), is divided into two parts. Part 'A' is implemented in the finite element method in a standard way through the constitutive law. Part 'B' represents strain softening, where stress decreases with increasing strain. It is modelled through the FDEM. For the sake of simplicity, the cracks are assumed to coincide with the element edges. Separation of these edges induces a bonding stresses Lisjak et al. (2013), which is taken to be a function of the size of separation δ or slip s (Fig. 1). Thus, separation of adjacent finite element edges implies crack opening δ and slip s.

In theory the separation $\delta = \delta_p = 0$ and slip $s = s_p = 0$ coincide with bonding stresses being equal to the tensile strength f_t and shear strength f_s respectively, i.e. no separation or slipping occur before the tensile or shear strengths are reached.

In this study, a modified version of the crack element constitutive response proposed by Munjiza et al. (1999) was adopted, Lisjak et al. (2013). The bonding stresses, σ and τ, transferred by the material are decreasing functions of the displacement discontinuity across the crack elements,

$$\begin{bmatrix}\sigma \\ \tau\end{bmatrix} = f(D) \begin{bmatrix}f_t \\ f_s\end{bmatrix}, \tag{7.1}$$

$f(D)$ is a heuristic scaling function representing an approximation of the experimental cohesive laws proposed by Evans and Marthe (1968),

$$f(D) = \left[1 - \frac{a+b-1}{a+b} \exp\left(D \frac{a+cb}{(a+b)(1-a-b)}\right)\right] \times \Big[a(1-D) + b(1-D)^c\Big], \tag{7.2}$$

where a, b, c, are parameters chosen to fit a particular experimental curve for concrete in tension, and D is a damage factor varying between 0 and 1. The dimensionless damage factor D describes the displacement jump across the cohesive surface.

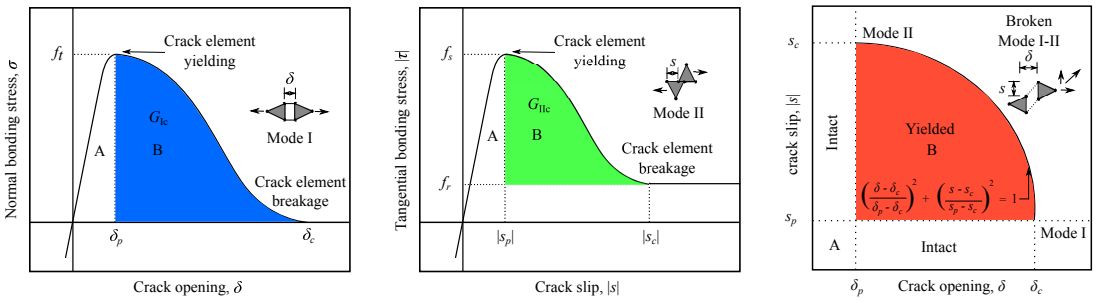

Figure 2: Constitutive behavior of the crack elements. (a) FPZ model for mode I. (b) Slip–weakening model for mode II. The specific fracture energy values, G_{Ic} and G_{IIc}, correspond to the area under the bonding stress–softening curves. The shape of the curves is based upon experimental complete stress–strain curves obtained for concrete in direct tension Evans and Marthe (1968). (c) Elliptical coupling relationship between crack opening δ and crack slip s for mixed–mode fracturing, eq. (7.7).

Also, $f(D)$ is such that $f(D=0)=1$ (i.e. intact crack element) and $f(D=1)=0$ (i.e. broken crack element). The actual fitting for one the experimental curves presented by Evans and Marthe (1968) is presented by setting $a=0.63$, $b=1.8$ and $c=6.0$ (Fig. 3).

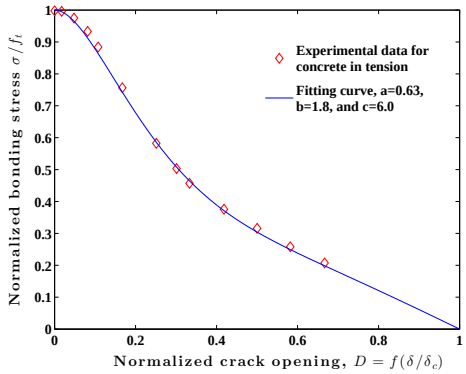

Figure 3: Paramterization of eq. 7.2 to fit the experimental behavior of concrete in tension as presented by Evans and Marthe (1968).

Depending on the local stress and deformation fields, fractures can nucleate and grow in mode I (i.e. opening mode), mode II (i.e. sliding mode) or in mixed mode I–II. Similar to the cohesive model originally proposed for concrete by Hillerborg et al. (1976), a mode I crack initiates when the crack tip opening, δ, reaches a critical value, δ_p, which is related to the cohesive tensile strength of the rock, f_t (Fig. 2(a)). As the fracture propagates and the crack tip opening increases, the normal bonding stress, σ, is assumed to decrease until a residual opening value, δ_c, is reached and a traction–free surface is created. In this case, the damage factor is therefore defined as,

$$D=\frac{\delta-\delta_p}{\delta_c-\delta_p}. \tag{7.3}$$

Mode II of fracturing is simulated by a slip–weakening model. A tangential/shear bonding stress, τ, exists between the two fracture walls, which is a function of the amount of slip, s, and the normal stress on the fracture, σ_n (Fig. 2(b)). The critical slip, s_p, corresponds to the cohesive shear strength of the rock, f_s, defined as,

$$f_s=c+\sigma_n\tan(\phi_i), \tag{7.4}$$

where c is the internal cohesion, ϕ_i is the material internal friction angle. Upon undergoing the critical slip, s_p, the tangential bonding stress is gradually reduced to a residual value, f_r, which corresponds to a purely frictional resistance,

$$f_r=\sigma_n\tan(\phi_f), \tag{7.5}$$

where ϕ_f is the fracture friction angle and σ_n is the normal stress acting across the fracture surfaces by the element pair interaction algorithm even after the breakage of the embedded crack element, see Mahabadi et al. (2012). In this case, the damage parameter is defined as,

$$D=\frac{s-s_p}{s_r-s_p}. \tag{7.6}$$

For mixed mode I–II of fracturing (Fig. 2(c)), the coupling between crack opening and slip is defined by an elliptical relationship,

$$D=\sqrt{\left(\frac{\delta-\delta_p}{\delta_c-\delta_p}\right)^2+\left(\frac{s-s_p}{s_r-s_p}\right)^2}. \tag{7.7}$$

As illustrated in (Fig. 4(b)), the effect of the crack bonding stress is implemented in FDEM using equivalent crack nodal forces, $\boldsymbol{f_c}$.

In actual implementation, the separation of adjacent element edges is assumed in advance through the topology of adjacent elements being described by different nodes. Thus no two elements share any nodes – the continuity between elements is enforced through the penalty function method, i.e. normal springs as shown in (Fig. 5).

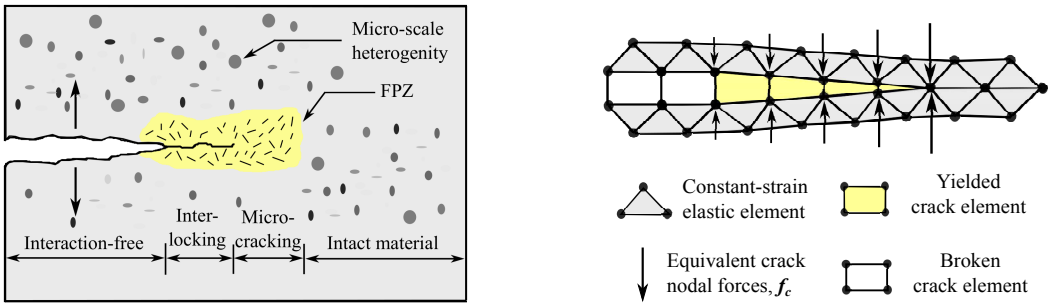

(a) (b)

Figure 4: Material failure modelling in FDEM (a) Conceptual model of a tensile crack in a heterogeneous rock material. (b) Theoretical FPZ model of Hillerborg et al. (1976).

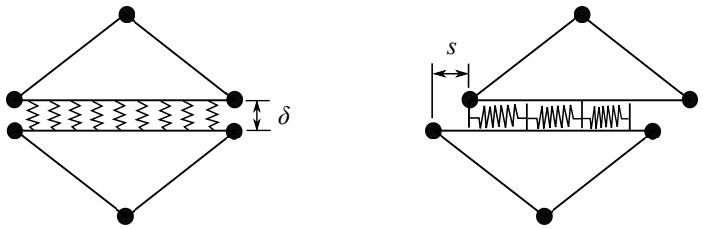

(a) (b)

Figure 5: Penalty method to ensure the connectivity between the generic elements of the FEM (a) Normal springs. (b) Shear springs.

Since the elastic deformation before the onset of fracturing takes place in the bulk material, no deformation should in theory occur in the crack elements before the cohesive strength is exceeded. However, a finite stiffness is required for the crack elements by the time–explicit formulation of FDEM. Such an artificial stiffness is represented by the normal, tangential and fracture penalty values, p_n , p_t and p_f, for compressive, shear and tensile loading conditions, respectively. For instance, for the normal separation δ, δ_p is defined as,

$$\delta_p = \frac{2h\, f_t}{p_f}, \tag{7.8}$$

and the slip s_p by,

$$s_p = \frac{2h\, f_s}{p_t}. \tag{7.9}$$

In the limits,

$$\lim_{p_{f,t}\to\infty} \delta_p,\ s_p = 0, \tag{7.10}$$

i.e. no separation or sliding between adjacent edges occurs before the tensile strength f_t of the material is reached. Thus, for practical purposes, the cohesive contribution to the overall model compliance can be largely limited by adopting very high (i.e. dummy) penalty values.

7.3 Governing equations

In FDEM, each solid is discretized as a mesh consisting of nodes and triangular elements. An explicit second–order finite–difference time integration scheme is applied to solve the equations of motion for the discretized system and to update the nodal coordinates at each simulation time step, Munjiza et al. (1995). In general, the governing equations for a FDEM system can be expressed as,

$$\mathbb{M}\ddot{\mathbb{X}} + \mathbb{C}\dot{\mathbb{X}} = \mathbb{R}(\mathbb{X}), \tag{7.11}$$

where $\mathbb{M}$ and $\mathbb{C}$ are the lumped mass and damping diagonal matrices of the system, $\mathbb{X}$ is the vector of nodal displacements and $\mathbb{R}$ is the nodal force vector which includes the contributions from the external loads $\boldsymbol{f_l}$, the interaction forces acting across discrete bodies $\boldsymbol{f_i}$, the deformation forces $\boldsymbol{f_e}$ and the crack bonding forces $\boldsymbol{f_c}$.

Numerical damping is introduced in the governing equation to account for energy dissipation due to non-linear material behaviour or to model quasi–static phenomena by dynamic relaxation, Lisjak et al. (2013). The matrix $\mathbb{C}$ is equal to,

$$\mathbb{C} = \mu \boldsymbol{I}, \tag{7.12}$$

where μ and $\boldsymbol{I}$ are the damping coefficient and the identity matrix, respectively.

Interaction forces $\boldsymbol{f}_{\mathbf{i}}$, are calculated either between contacting separated bodies or along internal discontinuities (i.e. pre–existing and newly created fractures). In the normal direction, body impenetrability is enforced using a penalty method Munjiza and Andrews (2000), while in the tangential direction, discontinuity frictional behavior is simulated by a Coulomb–type friction law, Mahabadi et al. (2012). Deformation forces $\boldsymbol{f}_{\mathbf{e}}$, are computed on an element–by–element basis under the assumption of isotropic linear elasticity. Crack bonding forces $\boldsymbol{f}_{\mathbf{c}}$, are used to simulate material failure as shown in (Fig. 4).

The failure of the material progresses based solely on the strength degradation of crack elements, which are inserted between each pair of triangular element edges at the beginning of the simulation. Crack elements occur where crack localization and growth take place. Since no adaptive remeshing is performed, potential fracture trajectories are restricted by the initial mesh topology. Therefore, to minimize the bias induced to the model response, fine and randomly discretized meshes should be used in place of structured grids. Following this approach, the macroscopic material failure emerges as a result of the collective crack–element damage without employing any additional macroscopic constitutive law. The key processes in FDEM include: elastic deformation of finite elements, rigid motion of discrete bodies, contact detection and interaction between discrete elements (including friction), and fracturing.

7.4 Numerical integration scheme

The integration scheme adopted in the Y–Geo code is an explicit second–order finite difference integration scheme. At each simulation time step, eq. (7.11) is integrated to update the nodal coordinates. For each node, the velocity at time $t + \Delta t$ (where Δt is the integration time step) is obtained as,

$$\dot{\mathbb{X}}^{t+\Delta t} = \dot{\mathbb{X}}^{t} + \frac{\boldsymbol{f}}{m}\,\Delta t, \tag{7.13}$$

where m is the nodal mass, and $\boldsymbol{f}$ is the vectorial sum of all forces applied to the node. Then, the updated nodal position is calculated as,

$$\mathbb{X}^{t+\Delta t} = \mathbb{X}^{t} + \dot{\mathbb{X}}^{t+\Delta t}\,\Delta t. \tag{7.14}$$

Since an explicit time integration scheme is adopted, the solver is conditionally stable. However, the time step size, Δt, must be smaller than a critical value, which is proportional to the smallest element size in the model divided by the P–wave velocity of the elastic medium, Lisjak et al. (2013).

7.5 Spatial discretization

In order for the bonding stress to have an effect on the stress field close to the crack tip, the size of the finite element h should be smaller than the estimated size of the plastic zone, Δ, given by eq. (7.15) and eq. (7.16)[1].

$$\Delta = \frac{E}{4f_t}\,\delta_c, \quad \text{short crack,} \tag{7.15}$$

and,

$$\Delta = \frac{\pi E \delta_c}{32 f_t}, \quad \text{short crack.} \tag{7.16}$$

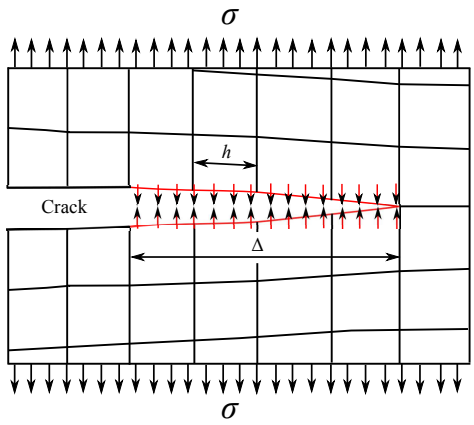

Figure 6: The maximum size of the finite element to capture the effect of bonding stress at the crack tip.

If the size of the finite elements, h, close to the crack tip is not small enough, the finite element mesh cannot accurately represent the stress field in the close proximity of the crack tip (Fig. 6). Consequently, the stress field at the crack tip will be influenced by the local mesh topology. Therefore,

$$h \ll \Delta. \tag{7.17}$$

For instance if the material is defined by $f_t = 3.15$ MPa, $E = 26$ GPa and $\delta_c = 0.238 \times 10^{-3}$ m, the rough estimate of the size of plastic zone, $Delta$, for a short crack in an infinite disc is given by eq. (7.15),

$$\Delta = \frac{E\,\delta_c}{4f_t} = \frac{26 \times 10^3 \times 0.238 \times 10^{-3}}{4 \times 3.15} = 0.491\,\text{m}, \tag{7.18}$$

while the rough estimate of the size of the plastic zone for a long crack in an infinite disc is given by eq. (7.16),

$$\Delta = \frac{\pi\,E\,\delta_c}{32 f_t} = \frac{\pi \times 26 \times 10^3 \times 0.238 \times 10^{-3}}{32 \times 3.15} = 0.193\,\text{m}. \tag{7.19}$$

Such a fine mesh results in the de–bonding process being driven by a smooth stress field averaged over several elements. In the case of a coarse mesh the de–bonding process may be defined by a stress state at just one element, (as explained earlier). This may result in a fracture pattern being dependent on the finite element mesh employed, i.e. the results obtained may differ significantly for different meshes.

[1] See Munjiza et al. (1999) for details.

7.6 Implementing hydraulic fracturing in the FDEM

The purpose of this section is to assess the use of an alternative hybrid finite–discrete element (FDEM) code, enhanced with hydraulic fracturing capabilities, to model pressure–driven fracturing in jointed rock masses. Numerical simulations will be carried out using this hybrid finite–discrete element (FDEM) code enhanced with hydraulic fracture (HF) capabilities. The simulation tool consists of three main computational modules exchanging information at every time step (Fig 7):

1. the geomechanics solver, based on the combined finite–discrete element method Munjiza (2004) and Mahabadi et al. (2012), captures the mechanical response of the rock mass (i.e. deformation and fracturing);
2. the cavity volume calculator dynamically tracks the evolution of wet fractures within the model and computes variations in cavity volume due to rock elastic deformation and fracturing as well as fluid compressibility;
3. the pump model computes the fluid pressure based on the injection flow rate and cavity volume.

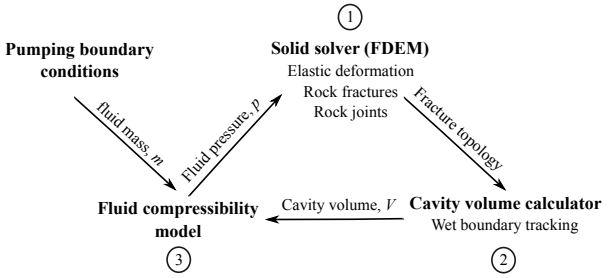

Figure 7: Hydro–mechanical coupling in the FDEM using the hydrostatic model, modified after Lisjak et al. (2014).

7.6.1 Geomechanics solver

In the geomechanics solver the solid rock is discretized as a mesh consisting of nodes and triangular elements (Fig. 4). An explicit second–order finite–difference integration scheme is applied to solve the equations of motion for the discretized system and to update the nodal coordinates at each simulation time step, Sect. (7.4).

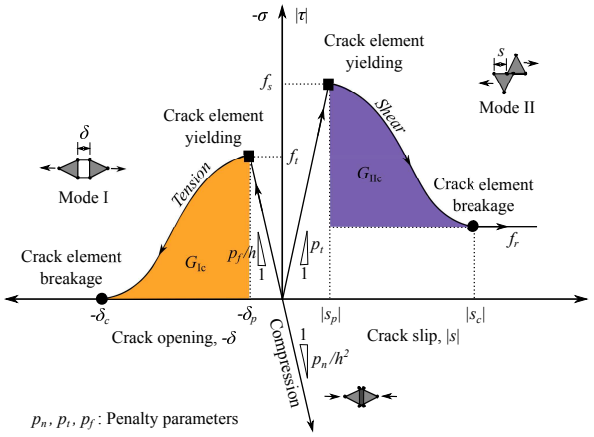

Figure 8: Constitutive behaviour at the contact between bonded triangular element pairs defined in terms of normal and tangential bonding stress, σ and τ, versus crack relative displacement, δ and s (i.e., opening and sliding).

7.6.1.1 Elastic deformation

The elastic deformation of the solid rock is modelled according to the continuum theory of linear elasticity using constant-strain triangular elements Munjiza (2004).

7.6.1.2 Rock fracture model

Rock fracturing is modelled using a cohesive–zone approach. With this technique, crack nucleation and growth is captured by dedicated four–noded interface elements (referred herein to as crack elements), that are interspersed across the edges of all triangular element pairs (Fig. 4). Since no adaptive remeshing is performed as the simulation progresses, potential fracture trajectories are restricted to the initial mesh topology. Therefore, to minimize the bias induced on the model response, randomly discretized meshes should be used in place of structured grids. In the crack element model, the bonding stresses transferred by the material are functions of the displacement discontinuity across the crack elements according to the cohesive laws illustrated in (Fig. 8).

7.6.1.3 Rock joint model

Rock discontinuities (i.e., either pre–existing or newly created fractures) are treated by a rock joint model, computing the contact forces between all pairs of triangular elements that overlap in space. Two types of forces are applied to the elements of each contacting pair: (i) repulsive forces and (ii) frictional forces. The repulsive forces are calculated using a penalty function. Contacting pairs tend to penetrate into each other, generating distributed contact forces, which depend on the shape and size of the overlap between the two bodies and the value of a stiffness parameter, namely the normal penalty coefficient,

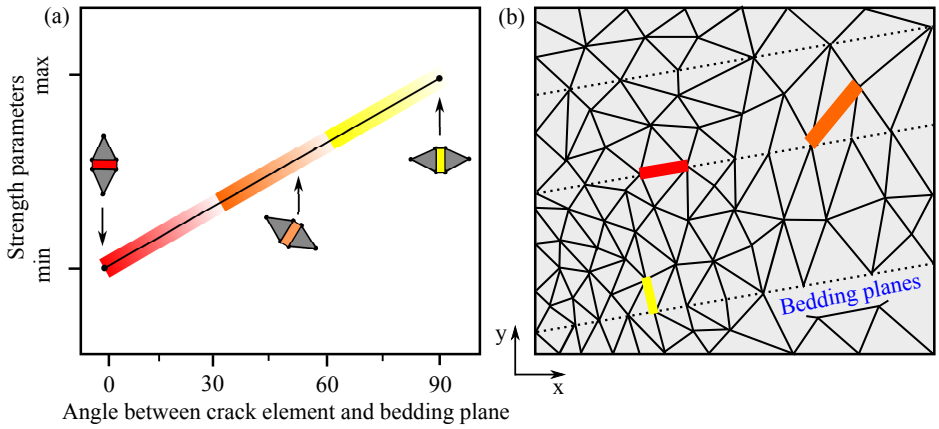

Figure 9: FDEM modelling of strength anisotropy. (a) Linear variation of cohesive strength parameters with the angle between crack element and bedding. (b) Example of mesh combining a Delaunay triangulation for the intra–layer material with edges preferentially aligned along the bedding plane direction, modified after Lisjak et al. (2014).

p_n. In the tangential direction, the frictional forces between contacting couples are calculated using Coulomb's law of friction. Rock joints can be directly incorporated into the geomechanics solver by aligning the mesh topology to pre–existing cracks at the time of mesh generation (Fig 9). In this study, rock joints are modelled as purely frictional surfaces. If at any time during the simulation a joint intersects a fluid–driven fracture, the resulting fluid percolation is accounted for by having the fluid pressure applied to the entire newly–connected discontinuity.

Following (Fig. 9), strength anisotropy is captured at the crack element level by assuming that the strength of each crack element is a function of its relative orientation with respect to the bedding orientation. That is to say, the macroscopically observed strength anisotropy is induced by a similar anisotropy at the crack element level. In this work, the cohesive strength parameters and the fracture energy release rates are assumed to vary linearly between a minimum value for orientations parallel to the bedding planes (i.e. $f_{t;\min}$, $c_{\min}$, $G_{\mathrm{Ic};\min}$, $G_{\mathrm{IIc};\min}$) to a maximum value for an orientation perpendicular to the bedding planes (i.e. $f_{t;\max}$, $c_{\max}$, $G_{\mathrm{Ic};\max}$, $G_{\mathrm{IIc};\max}$).

7.6.2 Fluid injection and pressure driven fracturing

Fluid injection and pressure–driven fracture propagation are captured by a simplified approach based on the principle of mass conservation for a compressible fluid injected into a deformable solid. The model is hydro–mechanically coupled exclusively in the sense that variations in cavity volume, due to either rock elastic deformation or fracturing, affect the pressure of the compressible fluid, which, in turn, affects rock deformation and failure (Fig. 7). On the other hand, the actual fluid flow, induced by hydraulic head gradients, in the fracture network and, depending on the permeability, in the rock matrix is neglected.

Prior to the start of the HF simulation, the boundary of the initial pressurized surface (typically coincident with the borehole perimeter) is specified by labelling the element edges adjacent to the fluid (Fig. 10). At each subsequent time step, a dedicated routine computes the cavity volume based on the fracture topology and inter–connectivity updated by the geomechanics solver.

Specifically, the volume is calculated according to Green's theorem by evaluating the following integral over the wet boundary,

$$V = \frac{1}{2} \oint x\, dy - y\, dx. \tag{7.20}$$

Numerically, this integration is calculated as,

$$V = \frac{1}{2} \sum_i x_i\, y_{i+1} - y_i\, x_{i+1}, \tag{7.21}$$

with i indexing over the nodes of the wet boundary with coordinates $(x_i,\, y_i)$. As the simulation progresses and the nucleation of new fractures is simulated, new wet edges are dynamically tracked based on their connectivity with the initial pressurized surface. The cavity volume calculated at each time step is fed into the pump model.

7.6.3 Fluid compressibility model/Pump model

The fluid compressibility model is used to determine the fluid pressure, p, to be applied to all edges marked as wet. In general, the fluid pressure depends on the input flow rate, Q, and responds to variations in cavity volume, V. At every time step, the mass, m, of the fluid is integrated from the flow rate (specified as a time–varying boundary condition/pumping boundary condition),

$$K_f = -V \frac{dp}{d\rho}, \tag{7.22}$$

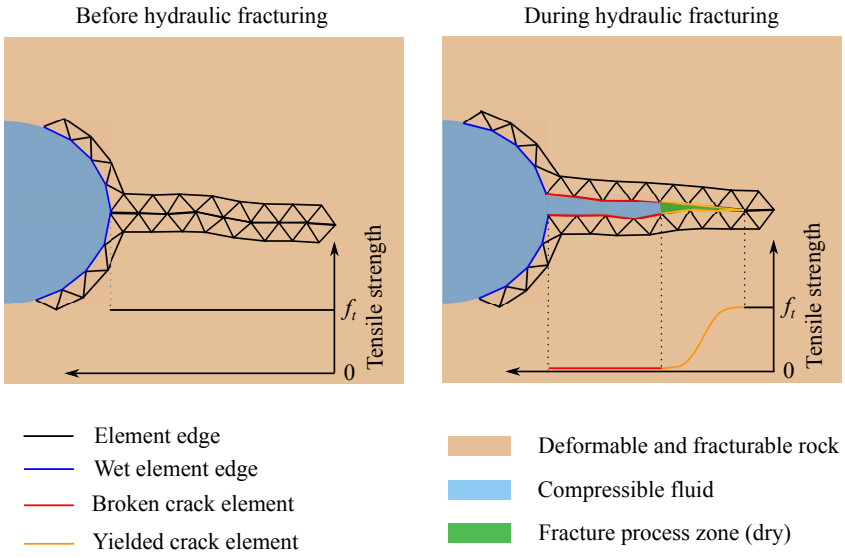

Figure 10: Conceptual diagram of the hydraulic fracture propagation process in a FDEM–HF model. For illustration purposes, only selected triangular elements are shown, modified after Lisjak et al. (2014).

with K_f being fluid bulk modulus. The pressure is therefore calculated as,

$$p = p_0 + K_f \log\left(\frac{m}{V\rho_0}\right), \tag{7.23}$$

where p_0 and ρ_0 are the reference fluid pressure and density respectively.

Based on the length and orientation of each wet element edge, the fluid pressure is converted into equivalent nodal forces $\boldsymbol{f}_{\mathrm{lf}}$, which are then added to eq. (7.11). Specifically, the fluid-pressure forces acting on two edge nodes, 0 and 1, are equal to,

$$\boldsymbol{f}_{\mathrm{lf}} = -\frac{p}{2}\begin{bmatrix} y_1 - y_0 \\ x_1 - x_0 \end{bmatrix}. \tag{7.24}$$

7.7 Concerns and limitations of the FDEM–HF model

In this section a brief discussion is presented about the limitations or concerns that can be encountered while using the FDEM–HF model to present hydraulic stimulation by the Y-Geo code.

7.7.1 Thermal strains

The injection of cold fluid into hot rocks laying deep in the earth's crust is expected to cause considerable thermal changes. Thermal changes lead to thermal strains that must be accounted for when calculating the effective stresses (McTigue (1986); AbuAisha and Loret (2014a); AbuAisha and Loret (2014b)). The mechanical behavior of a saturated porous medium subjected to a temperature change θ is expressed in a compact form as,

$$\boldsymbol{\sigma} + \kappa\, p\, \boldsymbol{I} = \boldsymbol{E} : (\boldsymbol{\varepsilon} - \boldsymbol{\varepsilon}^{\boldsymbol{\theta}}), \tag{7.25}$$

where $\boldsymbol{\sigma}$ is the total stress tensor, κ is the Biot's effective stress coefficient, $\boldsymbol{E}$ is the elasticity tensor, and $\boldsymbol{\varepsilon}^{\boldsymbol{\theta}}$ is the thermal strain tensor defined as $\varepsilon^{\theta}_{ij} = (\alpha_s/3)\,\theta\,\delta_{ij}$, with α_s being the rock cubical thermal expansion coefficient. For typical sandstone values ($E = 5$ GPa, $\nu = 0.3$, $\alpha_s = 4.5 \times 10^{-5}$ 1/°C) and from the correspondence between thermoelasticity and poroelasticity, one writes:

$$\kappa\,(1 - 2\nu)\,\Delta p \Longleftrightarrow -\frac{E\,\alpha_s\,\theta}{3}. \tag{7.26}$$

For a typical injection test the change of temperature θ is up to -80 °C (cooling) which is equivalent to fluid pressure change of 15 MPa ($\kappa = 1$ for effective stresses at the fracture tip)[2]. This indicates that the cooling effects taking place at the beginning of an injection test can be equivalent to large pressurizing values. If the injection process is going to be implemented with small fluid volumes and at quite short periods, the effect of heat shock is to be analyzed as well. The numerical stabilization of heat convection at early injection times is presented in the work of (AbuAisha (2014), ch. 6).

The equation of balance of momentum, also called the equilibrium equation of elasticity, is derived based on Newton's law of motion which states that: in an initial frame of reference, the material rate of change of the linear momentum of a body is equal to the resultant applied forces. Consequently, to account for the balance of a porous medium subjected to external me-

[2]Refer to (AbuAisha (2014), p. 124) to understand the derivation of the relation (7.26).

chanical loads and thermal exchanges eq. (7.25) is employed,

$$\boldsymbol{\nabla}.\boldsymbol{\sigma} + \boldsymbol{b} = \rho\dot{\boldsymbol{v}}, \tag{7.27}$$

where $\boldsymbol{b}$ is the body forces, ρ is the density of the current configuration and $\dot{\boldsymbol{v}}$ is the acceleration.

7.7.2 Fluid diffusion in a porous medium

The approach adopted in developing the Y–Geo code to simulate fluid–driven–fractures does not account for fluid diffusivity in the porous medium, nor does it consider fluid leak–off from the fracture walls, Sect. (7.6). The constitutive equation of Darcy (7.28) relates the apparent flux of fluid to pressure gradient and is used to describe the diffusion of fluid in the porous medium.

$$\boldsymbol{q}_f = \phi_0(\boldsymbol{v}_f - \boldsymbol{v}_s) = -\frac{\boldsymbol{k}}{\mu}.(\boldsymbol{\nabla}p - \rho_f\,\boldsymbol{g}), \tag{7.28}$$

where $\boldsymbol{q}_f$ is the apparent volumetric flux of the fluid relative to the solid skeleton, $\boldsymbol{v}_f$ is the fluid velocity, $\boldsymbol{v}_s$ is the solid velocity, $\boldsymbol{k}$ is the permeability tensor of the mixture, μ is the dynamic fluid viscosity, ρ_f is the intrinsic fluid density, and $\boldsymbol{g} = g\,\boldsymbol{e_3}$, g is the gravitational acceleration and $\boldsymbol{e_3}$ is the descending vertical direction.

To account for the amount of fluid entering or leaving the fractures. The linearized fluid mass balance equation according McTigue (1986) is used,

$$\frac{\partial\zeta}{\partial t} + \nabla.\boldsymbol{q}_f = 0, \tag{7.29}$$

where ζ is the change in the fluid content. According to McTigue (1986) the change in mixture fluid content constitutive equation can be expressed as,

$$\zeta = \frac{1}{3}\left(\frac{1}{K} - \frac{1}{K_s^{'}}\right)(\sigma_{kk} + \frac{3}{B}\,p), \tag{7.30}$$

with K being the drained bulk modulus of the porous medium, $K_s^{'}$ is the first solid constituent bulk modulus, and B is the pore pressure (Skempton's) coefficient given by,

$$\frac{1}{B} = 1 + \phi_0\frac{K(1 - K_f/K_s^{''})}{K_f(1 - K/K_s^{'})}, \tag{7.31}$$

$K_s^{''}$ is the second solid constituent bulk modulus and ϕ_0 is the reference porosity of the mixture.

Assuming that $K_s^{'} = K_s^{''} = K_s$ leads to the definition of Biot's modulus M,

$$\frac{1}{M} = \frac{\kappa - \phi_0}{K_s} + \frac{\phi_0}{K_f}. \tag{7.32}$$

Thus eq. (7.30) takes the form Abousleiman and Ekbote (2005),

$$\zeta = \frac{p}{M} + \kappa\,\varepsilon_{kk}. \tag{7.33}$$

The effective stress (Biot's) coefficient κ is expressed in terms of bulk moduli as,

$$\kappa = \frac{K_s^{'} - K}{K_s^{'}}, \tag{7.34}$$

the difference between the bulk moduli $K_s^{'}$ and $K_s^{''}$ is usually ascribed to the presence of unconnected porosity.

7.7.2.1 Time scale associated with fluid diffusion in porous media

The time scale associated with diffusive flow of the pore fluid is given by $t_p = L^2/C_c$, C_c is the consolidation coefficient (m^2/s) and is defined as $C_c = k\,(\lambda + 2G)/\mu$, k is the permeability of the medium (m^2), μ is the dynamic viscosity of the pore fluid (N.s/m^2), λ & G are Lamé's elastic constants (N/m^2), and L is a typical length of the Boundary Value Problem (BVP) considered (m).

For typical granitic rocks, the drained Young's modulus E is around 40 GPa, the drained Poisson's ratio ν is around 0.2, and the permeability k is in the order of 10^{-14} m^2. The Lamé's coefficients are now calculated as,

$$G = \frac{E}{2(1+\nu)} = \frac{40}{2(1+0.2)} = 16.67 \text{ GPa, and,} \tag{7.35}$$

$$\begin{aligned}\lambda &= \frac{E\nu}{(1+\nu)(1-2\nu)} = \frac{40\times 0.2}{(1+0.2)(1-2\times 0.2)} \\ &= 11.11 \text{ GPa.}\end{aligned} \tag{7.36}$$

Knowing that the dynamic viscosity of water at temperature of 30 °C is around 8.0×10^{-4} Pa.s, the consolidation coefficient,C_c, can be calculated,

$$\begin{aligned}C_c &= \frac{k\,(\lambda+2G)}{\mu} \\ &= \frac{5\times10^{-14}\times(16.67+11.11)\times10^9}{8.0\times10^{-4}} = 1.74 \text{ m}^2\text{/s}\end{aligned} \tag{7.37}$$

The hydraulic fracturing process may last up to 50 minutes on average. Consequently, the region affected by the diffusion of fluid can reach up to:

$$L = \sqrt{C_c\,t_p} = \sqrt{1.74\times50\times60} \approx 72 \text{ m.} \tag{7.38}$$

Following the result of eq. (7.38), the diffusivity of pore fluid in the porous medium will depend on the dimensions of the BVP simulated by the Y-Geo code. Based on the authors' experience (AbuAisha and Loret (2014a); AbuAisha and Loret (2014b)), the area affected by the fluid diffusion can extend up to $L\times3/2 = 108$ m in 50 minutes. Even though the fluid diffusivity in the porous medium is questionable depending on the time of stimulation, the leakage of fluid from the fracture surfaces is quite possible even at small stimulation periods.

7.7.2.2 Fluid leak–off from the fracture surfaces

Let us assume that we have a vertical borehole where pressurized fluid is injected into a horizontal reservoir to the threshold of HF. The plane strain approximation is used to treat a horizontal section of a vertical fracture as shown in (Fig. 11). The fluid leak–off is assumed one–dimensional occurring perpendicular to the fracture walls.

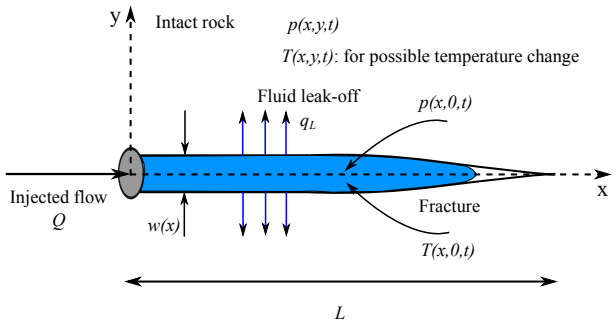

Figure 11: Horizontal section of a vertical fracture in a stimulation test. Fluid leak-off is assumed one–dimensional occurring perpendicular to the fracture walls. T refers to the fluid and solid rock temperatures, it is included in the graph in case that thermal strains are to be considered due to considerable thermal changes.

Assuming that the fracture aperture is small and varies slowly in space and time and that the flow in the fracture is laminar, the lubrication flow theory applies (Lamb (1945); Ghassemi et al. (2008)). Momentum balance for these assumed conditions indicate that the flow rate is proportional to the pressure gradient, i.e.,

$$\frac{\partial p(x,0,t)}{\partial x} = -\frac{12\mu}{w^3(x,t)}\, q(x,t), \tag{7.39}$$

where p is the fluid pressure increase in the fracture caused by injection ($p = p(x,0,t) - p_0$) with p_0 being the initial reservoir pressure, w is the fracture aperture, and q is the flow rate per unit height of a vertical fracture: $q(x,t) = w(x,t)\, v_f(x,t)$, where v_f is the average fluid speed in the fracture.

Assuming the fluid to be incompressible with leak–off from the fracture wall into the formation, the fluid continuity equation reads,

$$\frac{\partial q(x,t)}{\partial x} = -2q_L(x,t), \tag{7.40}$$

where $q_L(x)$ is the leak–off speed (positive for loss into the formation). The coefficient 2 is due to the fact that both fracture walls are considered. Combining Eqs. (7.39) and (7.40), and neglecting $\partial w/\partial x$, the following second–order partial differential equation is obtained for fluid pressure in the fracture,

$$\frac{\partial^2 p(x,0,t)}{\partial x^2} = \frac{24\mu}{w^3(x,t)}\, q_L(x,t). \tag{7.41}$$

The amount of the fluid leakage, as well as possible fluid diffusion in the porous medium should be considered during the simulation of HF test.

Eqs. (7.27) and (7.29) can be solved analytically for a mathematical model based on an idealized geometry. Let us assume a horizontal reservoir of constant thickness, confined at the top and the bottom by rigid, impermeable and thermally insulated formations; the reservoir can be of finite or infinite extent. The fracture is modelled as a vertical plane of uniform width that intersects the entire reservoir thickness, see (Fig. 12) for details. Plane strain and one–dimensional fluid leakage assumptions are also adopted as mentioned above in our approach.

To be able to obtain the analytical solution of the BVP, we shall assume, in our simplified approach, the rock displacement to be zero in the x-direction (parallel to the fracture). Furthermore, the influence of rock matrix deformation on pore pressure is not to be included as its impact is not major in the our context. The following initial boundary conditions are employed to describe fluid diffusion in the fracture as well as in the rock matrix:

1. Initial reservoir pressure is equal to zero, i.e. $p(x,y,0) = 0$ MPa,
2. the pore fluid pressure at the extraction well is equal to zero, i.e. $p(L,0,t) = 0$, and,
3. the initial fluid pressure at the injection well for an injection rate of $q_0 = 1.0 \times 10^{-4}$ m/s, is equal to $p_0 = 1.2$ MPa.

Solving analytically the poroelastic equations for the BVP described above, the following expressions for the development of the fracture aperture,

$$w(x,t) = \frac{2\eta K_1^D \sqrt{c_D\, t}}{G\sqrt{\pi}}(L^2 - x^2) + w_0, \tag{7.42}$$

fracture and reservoir pressure for constant aperture $w = w_0$,

$$p(x,y,t) = (x-L)(K_1^D(x+L) - K_2^D)\,\mathrm{erfc}\left(\frac{y}{2\sqrt{c_D t}}\right), \tag{7.43}$$

and fluid pressure change in the fracture due to varying aperture w,

$$p(x,0,t) = -12 q_0 \mu \int_0^x \frac{1}{w^3(x,t)}, \tag{7.44}$$

are obtained. q_0 is the injection flow rate per unit height of the fracture, c_D is the hydraulic diffusivity, and w_0 is the initial fracture aperture. The coefficient K_1^D is related to the fluid leak–off by the relation: $K_1^D = 12\mu\, q_{L0}/w_0^3$, meanwhile the coefficient K_2^D is related to the injection flow by the relation: $K_2^D = 12\mu\, q_0/w_0^3$. Fluid leak–off can be calculated using the following expression: $q_{L0} = m\, q_0/2L$ with m being the coefficient of leak–off and L being the length of the fracture. The parameter η is related to Biot's effective stress coefficient using Poisson's ratio as: $\eta = \kappa(1-2\nu)/2(1-\nu)$.

For typical reservoir operating conditions, the following data set, Table (1) is used in the BVP described above:

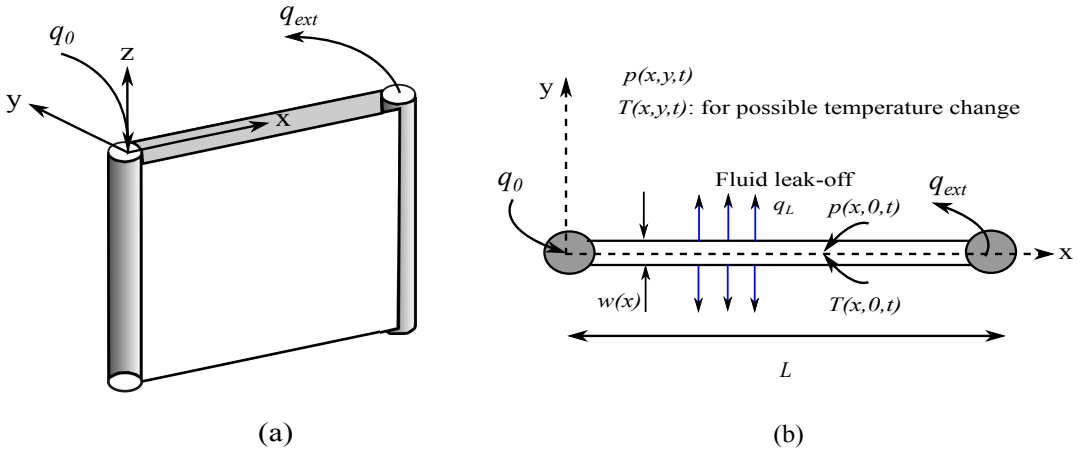

Figure 12: Side (a) and top (b) view of the system being modeled Ghassemi et al. (2008). The reservoir is assumed to extend from the top to the bottom of the system. The vertical fracture intersects the entire reservoir and extends between the injection well on the left and the production well on the right.

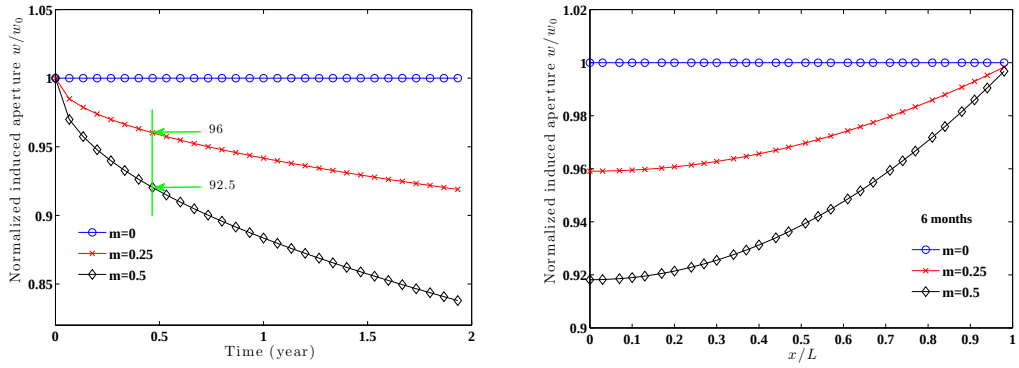

Figure 13: Normalized poroelastic-induced fracture aperture: (a) at the injection point for different fluid loss/injection rate ratios m and times; (b) along the fracture for different fluid loss/injection rate ratios m after 6 months of injection.

Table 1: Rock and fluid properties for a fracture fluid circulation test of the BVP defined above.

Parameter	Value	Unit
Injection rate, q_0	1.0×10^{-4}	m^2/s
Initial aperture, w_0	0.001	m
Poisson's ratio, ν	0.185	-
Dynamic fluid viscosity, μ	0.001	Pa.s
Fracture length, L	1000	m
Leak–off rate, q_{L0}	$mq_0/2L$	m/s
Hydraulic diffusivity, c_D	2.2×10^{-5}	m^2/s
Shear modulus, G	27.5	GPa

(Fig. 13(a)) shows that the fracture aperture is reduced more with increasing fluid loss ($m > 0$). The reduction in fracture aperture resulting from poroelastic deformation associated with fluid leak–off is plotted in (Fig. 13(b)) along the fracture for different values of m, and a time of 6 months. The contraction of the fracture opening is small in magnitude and evolves slowly in this case. The maximum reduction of aperture occurs at the injection point where the induced pressure $p(x, 0, t)$ has its maximum.

(Fig. 14) shows the pressure distribution in the fracture corresponding to the case illustrated in (Fig. 13(b)); the pressure is normalized with respect to the isothermal impermeable initial fracture pressure of 1.2 MPa.

Leak–off alone lowers the pressure in the fracture, but the pressure profiles for the poroelastic case (varying w) are higher than for the elastic case (constant $w = w_0$) with leak-off because of the poroelastic aperture contraction. As the poroelastic aperture changes become negligible near the extraction point (Fig. 13(b)), the poroelastic and elastic pressure profiles become

nearly identical. Fluid loss alone tends to decrease the fluid pressure in the fracture; as the amount of fluid loss increases, the pressure in fracture decreases, and the profile becomes more parabolic. It should be noted that although leak–off might not greatly change fracture aperture, it can lead to significant pore pressure changes and cause slip on fractures in the vicinity of the main hydraulic fracture system (i.e., operationally induced microseismicity).

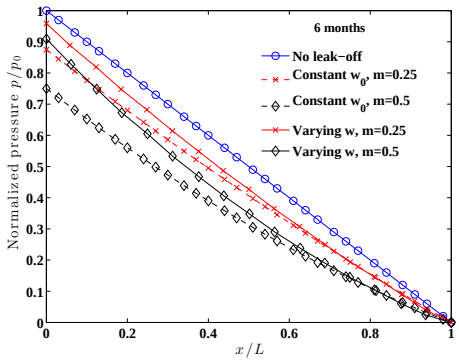

Figure 14: Normalized pressure profile along the fracture for different fluid loss/injection rate ratios m after 6 months of injection. Solid lines: elastic case (constant $w = w_0$); dashed lines: poroelastic case (varying w).

A typical time scale for a HF treatment stage is 50 minutes. Following (Fig. 13(a)), the reduction in fracture aperture due to leak–off is not going to be significant (around $\sim 8\%$ in 6 months). However, and as stated above, this insignificant reduction can lead to significant pore pressure increase, i.e. diffusion in the rock matrix.[3].

7.8 Conclusion

The Finite/Discrete Element Method (FDEM) has been presented in the framework of describing hydraulic fracturing in petroleum industry. General overview about the method is first presented. The limitations and concerns for applying the method to describe microseismicity are also discussed. If the method is to be applied to our future research, a special model to describe fluid diffusion in the porous skeleton must be accounted for.

7.9 Acknowledgments

The authors would like to thank the sponsors of the Microseismic Industry Consortium and NSERC for their financial support. The authors feel indebted to the original developers/source of the respective codes (Y-Geo and GEOS); specifically thanking Giovanni Grasselli and Scott Johnson for their assistance in implementing them.

7.10 References

Abousleiman, Y. and Ekbote, S., 2005, Solutions for the inclined borehole in a porothermoelastic transversely isotropic medium: International Journal for Numerical Methods in Engineerin, **72**,102–114.

AbuAisha, M., 2014, Enhanced geothermal systems: Permeability stimulation through hydraulic fracturing in a thermo–poroelastic framework: PhD thesis, Université de Grenoble.

AbuAisha, M. and Loret, B., 2014a, Enhanced Geothermal Systems (EGS): Hydraulic fracturing in a thermo-poroelastic framework: Computers and Geotechnics, IN PRESS.

AbuAisha, M. and Loret, B., 2014b, Influence of hydraulic fracturing on impedance and efficiency of thermal recovery from HDR reservoirs: Geothermics, IN PRESS.

Evans, P. H. and Marthe, M. S., 1968, Microcracking and stress-strain curves for concrete in tension: Materials and structures, **1**, 61–64.

Ghassemi, A., Nyrgen, A., and Cheng, A., 2008, Effects of heat extraction on fracture aperture: A poro-thermoelastic analysis: Geothermics, **37**, 525–539.

Hillerborg, A., Modeer, M., and Petersson, P. E., 1976, Analysis of crack formation and crack growth in concrete by means of fracture mechanics and finite elements: International Journal of Geomechanics, **6**, 773–782.

Lamb, H., 1945, Hydrodynamics: Sixth ed. Dover Publications, New York, NY, USA, 738 pp.

Lisjak, A., Liu, Q., Zhao, Q., Mahabadi, K. O., and Grasselli, G., 2013, Numerical simulation of acoustic emission in brittle rocks by two–dimensional finite–discrete element analysis: Geophysical Journal International, **DOI: 10.1093/gji/ggt221**.

Lisjak, A., Mahabadi, O. K., Kaifosh, P., Vietor, T., Grasselli, G., 2014, A preliminary evaluation of an enhanced FDEM code as a tool to simulate hydraulic fracturing in jointed rock masses: Alejano LR, Perucho A, Olalla C, Jimenez RS, editors. Rock engineering and rock mechanics: structures in and on rock masses. Leiden: CRC Press; p. 1427–32.

Lu, T.,Chow, C., 1990, A modified dugdale model for crack tip plasticity and its related problems: Engineering Fracture Mechanics, **37**, no. 3, 551–568.

Mahabadi, O. K., Lisjak, A., Munjiza, A., and Grasselli G., 2012, Y-Geo: a new combined finite-discrete element numerical code for geomechanical applications: International Journal of Geomechanics, **12**, no. 6, 676–688.

McTigue, D. F., 1986, Thermoelastic response of fluid–saturated porous rock: International Journal for Numerical Methods in Engineerin, **91**, 9533–9542.

Munjiza, A., 2004, The Combined Finite-Discrete Element

[3]Thermal effects should be considered if fluid injection is expected to cause considerable thermal changes.

Method: John Wiley & Sons Ltd, Chichester, West Sussex, England.

Munjiza, A. and Andrews, K. R. F., 2000, Penalty function method for combined finite–discrete element systems comprising large number of separate bodies: International Journal for Numerical Methods in Engineerin, **49**, no. 11, 1495–1520.

Munjiza, A., Andrews, K., and White, J., 1999, Combined single and smeared crack model in combined finite-discrete element analysis: International Journal for Numerical Methods in Engineering, **44**, no. 1, 41–57.

Munjiza, A., Owen, D. R. J., and Bicanic, N., 1995, A combined finite-discrete element method in transient dynamics of fracturing solids: Engineering Computations, **12**, no. 2, 145–174.